033256-1-T

COMPUTATION OF NOSE RADOME SCATTERING BY EMPLOYING THE FAST MULTIPOLE METHOD

S.S. Bindiganavale and J.L. Volakis

Naval Air Warfare Center Weapons Div.
China Lake, CA 93555-6001

December 1995

33256-1-T = RL-2455

Report #033256-1-T

Project Title:	Code Optimization and Radome De-Polarization Effects
Report Title:	Computation of Nose Radome Scattering by the Fast Multipole Method
Report Authors:	S. S. Bindiganavale and John L. Volakis
University Collaborator:	John L. Volakis
Navy Colaborator:	T.G.H.(Helen) Wang Code 472210D, Bldg. 01400 Naval Air Warfare Center Weapons Division China Lake, CA 93555-6001
University Address:	Radiation Laboratory Department of Electrical Engineering and Computer Science Ann Arbor, Michigan 48109-2122
Date:	December 1995

Computation of nose radome scattering by employing the fast multipole method to calculate the RCS of large objects

Radiation Laboratory
Department of Electrical Engineering and Computer Science
The University of Michigan
Ann Arbor, MI 48109-2122

Abstract

In this report we consider the computation of electromagnetic scattering by electrically large dielectric nose radomes. The surface of the radome is modeled using planar triangular patches and the fast multipole method (FMM) is applied to the electric field integral equation (EFIE) for the solution of the discrete system. By virtue of the FMM's $O(N^{1.5})$ operation count per iteration substantial solution speed ups and memory reductions are achieved and therefore the method can be used to model realistic size radomes. Results from typical nose radome geometries are presented along with validation data. For very large geometries, comparison is provided with a body of revolution code. Several calculations are presented and some of these include the interaction of the antenna with the nose radomes and demonstrate the effect of the radome on the antenna pattern.

1 Introduction

Nose radomes serve as enclosures for antennas and are generally pointed to reduce aerodynamic drag. The performance of a radome is generally described by parameters [1] which include the far-field radiation pattern, power transmittance, boresight error and boresight error slope. Approximate methods for treating the propagation of the plane wave through a radome include high frequency techniques which typically consider the radome to be locally plane and omit guided waves as well as interactions between the radome sections. Also, treatments of the higher order interactions between the radome and the antenna have so far been of little attention. Clearly, a more accurate approach is to employ an exact analysis method such as the moment method technique [2] which is capable of including all first and higher order phenomena. However, due to the traditional $O(N^2)$ storage and $O(N^3)$ CPU requirements the method of moments approach can only be used for small radome structures. Recently though techniques have been introduced which can reduce the CPU requirements down to $O(N^{1.5})$ or less for large scale simulations. The fast multipole method (FMM) [3] is one of these techniques and accomplishes the CPU reduction by lumping the far zone moment method elements into groups. The groups are subsequently interacted (rather than the elements) to achieve the purported CPU reduction. In the FMM implementation, the near-zone and self-cell elements are evaluated unaltered and thus the accuracy of the original method of moments formulation is retained.

2 Formulation

For this application, the thin dielectric radomes were modeled using the resistive boundary condition [4]

$$\hat{n} \times (\mathbf{E}^i + \mathbf{E}^s) = \eta_0 R \mathbf{J} \tag{1}$$

where R is the resistivity, $\mathbf{J}$ is the surface current, and $\mathbf{E}^i$ is the incident field which is a plane wave of unit amplitude given by

$$\mathbf{E}^i \;=\; (\hat{\theta}\cos\alpha + \hat{\phi}\sin\alpha)\, e^{jk_o(x\sin\theta_i\cos\phi_i + y\sin\theta_i\sin\phi_i)} \tag{2}$$

where k_0 is the free space wavenumber, α is the polarization angle and (θ_i, ϕ_i) indicate the direction of incidence. The scattered field $\mathbf{E}^s$ can be determined from **J** according to

$$\mathbf{E}^s = -j\omega\mathbf{A} - \nabla\phi \tag{3}$$

where the magnetic vector potential **A** is given by

$$\mathbf{A}(\mathbf{r}) = \frac{\mu_o}{4\pi}\int_S \mathbf{J}(\mathbf{r}')\frac{e^{-jk_oR}}{R}\,dS' \tag{4}$$

with S being the surface of the body. The scalar potential ϕ is given by

$$\phi(\mathbf{r}) = \frac{1}{4\pi\epsilon_o}\int_S \sigma(\mathbf{r}')\frac{e^{-jk_oR}}{R}\,dS'. \tag{5}$$

where R is the distance between observation and source points given by

$$R = |\mathbf{r} - \mathbf{r}'| = \sqrt{(x-x')^2 + (y-y')^2 + (z-z')^2} \tag{6}$$

The continuity equation is used to relate the surface charge density and the current

$$\nabla_s \cdot \mathbf{J} = -j\omega\sigma \tag{7}$$

Enforcing (1) on S yields the electric field integral equation for **J**

$$\mathbf{E}^i_{tan} = (j\omega\mathbf{A} + \nabla\phi)_{tan} + \eta_o R\,\mathbf{J} \quad \mathbf{r} \;\; on \;\; S \tag{8}$$

To model the current, the scatterer is discretized into triangular patches. The current is expanded in terms of vector basis functions [5] which are especially suited to triangular domains. Each basis function is associated with an interior (nonboundary) edge, and is nonzero only on the two triangles sharing that edge. Figure 1 shows the nth interior edge shared by triangles T_n^+ and T_n^- of area A_n^+ and A_n^- respectively. A point in the triangle pair can be designated by either the global position vector **r**, or local position vectors $\overline{\rho_n}^{\pm} = \mathbf{r} - \mathbf{r}^{\pm}$. The basis function $\mathbf{f}_n(\mathbf{r})$ for the n^{th} edge is defined as

$$\mathbf{f}_n(\mathbf{r}) = \begin{cases} \frac{l_n}{2A_n^+}\overline{\rho_n^+}, & \mathbf{r} \;\; in \;\; T_n^+ \\ \frac{l_n}{2A_n^-}\overline{\rho_n^-}, & \mathbf{r} \;\; in \;\; T_n^- \\ 0, & \text{otherwise} \end{cases} \tag{9}$$

The current **J** on S is approximated by

$$\mathbf{J} \cong \sum_{n=1}^{N} I_n\mathbf{f}_n(\mathbf{r}) \tag{10}$$

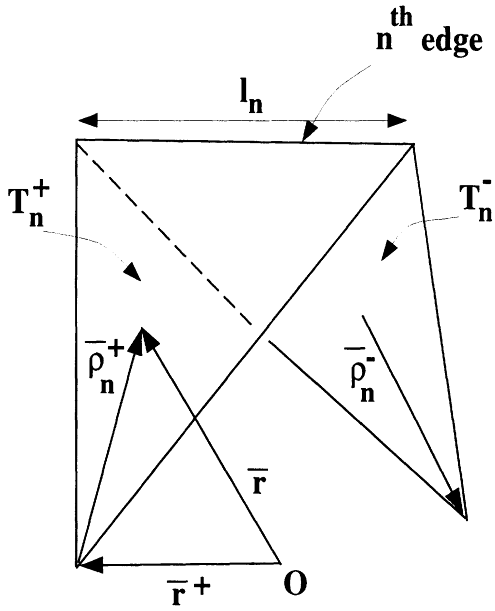

Figure 1: Local coordinates for the nth edge

where N is the number of interior edges and the unknown coefficients I_n represent the current density flowing across the n^{th} edge of the mesh which is showed by the T_n^+ and T_n^- triangles.

2.1 Integral equation solution

To solve for the basis coefficients, Galerkin's technique is applied to (8) obtaining

$$\int_S \mathbf{E}_i \cdot \mathbf{f}_m \, dS = j\omega \int_S \mathbf{A} \cdot \mathbf{f}_m \, dS - \int_S \phi \nabla_s \cdot \mathbf{f}_m \, dS + \eta_o \int_S R\mathbf{J} \cdot \mathbf{f}_m \, dS \,, \quad m = 1, ..., N. \tag{11}$$

Using (9) in (11) yields the $N \times N$ system of linear equations, $V = ZI$ where I_n is the N^{th} basis coefficient, Z_{mn} is the impedance matrix whose elements are computed from

$$
\begin{aligned}
Z_{mn} &= \frac{\eta_o l_m l_n}{4}\left\{\frac{j}{2}\int_{T_m^{\pm}}\int_{T_n^{\pm}} \frac{1}{A_m^{\pm}A_n^{\pm}}\,\rho_m^{\pm}(\mathbf{r})\cdot\rho_n^{\pm}(\mathbf{r}')\,\frac{e^{-jk_oR}}{R}\,dS'dS\right. \\
&- \frac{j}{2\pi^2}\int_{T_m^{\pm}}\int_{T_n^{\pm}} \frac{\epsilon_m\epsilon_n}{A_m^{\pm}A_n^{\pm}}\,\frac{e^{-jk_oR}}{R}\,dS'dS \\
&+ \left.\int_{T_m^{\pm}} \frac{R_n^{\pm}}{A_m^{\pm}A_n^{\pm}}\,\rho_m^{\pm}(\mathbf{r})\cdot\rho_n^{\pm}(\mathbf{r})\,dS\right\} \qquad (12)
\end{aligned}
$$

where ϵ_m and ϵ_n are the positive current reference signs for edges m and n, defined as

$$
\epsilon_m = \begin{cases} +1 & \mathbf{r}\ in\ T_m^{+} \\ -1 & \mathbf{r}\ in\ T_m^{-} \end{cases} \qquad (13)
$$

and

$$
\epsilon_n = \begin{cases} +1 & \mathbf{r}'\ in\ T_n^{+} \\ -1 & \mathbf{r}'\ in\ T_n^{-} \end{cases} \qquad (14)
$$

The integrals defining Z_{mn} are evaluated for near and self cells by the techniques detailed in [6]. The elements of the excitation vector are given by

$$
\begin{aligned}
V_m &= \frac{l_m}{2}\int_{T_m^{\pm}} \frac{\rho_m^{\pm}(\mathbf{r})}{A_m^{\pm}}\cdot(\hat{\theta}\cos\alpha + \hat{\phi}\sin\alpha) \\
&\quad e^{jk_o(x\sin\theta_i\cos\phi_i + y\sin\theta_i\sin\phi_i)}\,dS. \qquad (15)
\end{aligned}
$$

The $N \times N$ linear system can be solved either by direct methods such as matrix factorization (which would mean an execution time of $O(N^3)$) or iterative methods involving an operation count of $O(N^2)$/iteration. To make use of the FMM to speed-up the solution it is necessary to employ iterative methods. In this case it has been shown that the FMM [7] can reduce the operation count down to $O(N^{1.5})$/iteration, a substantial reduction. A detailed study of the parameters affecting the accuracy and solution time of this method is given in [8]. To employ the approximate version of the FMM, the unknowns are divided into groups with M unknowns in each group and thus the number of groups will then be $\frac{N}{M}$. For large source to observation distances, the kernel in (12) is approximated by using the large argument expansion as

$$
\frac{e^{-jk_0R}}{R} \sim e^{-jk_0\hat{r}_{l'l}\cdot\mathbf{r}_{li}}\,\frac{e^{-jk_0 r_{l'l}}}{r_{l'l}}\,e^{-jk_0\hat{r}_{l'l}\cdot\mathbf{r}_{jl'}} \qquad (16)
$$

where $r_{l'l}$ is the distance between the center of the test group l and the center of the source group l'; $r_{jl'}$ is the distance between the jth source element and its group center and r_{li} is the distance between the ith test element and its group center (see figure 2). It is important to note that for large source to observation distances integration over the triangular domains is accomplished by mid-point integration; thus the source and observation co-ordinates in (12) are replaced by the centroid of the triangular domain of integration. Also, while the magnitude terms represented by the basis functions are more easily approximated because of their non-oscillatory nature, the phase term in the kernel needs to be accurately computed. The decoupling of test-source element interactions in the kernel as in (16) enables the computation of the matrix-vector product for far-field groups with a reduced operation count as detailed in the following sequence, where we have considered only the oscillatory term in the kernel.

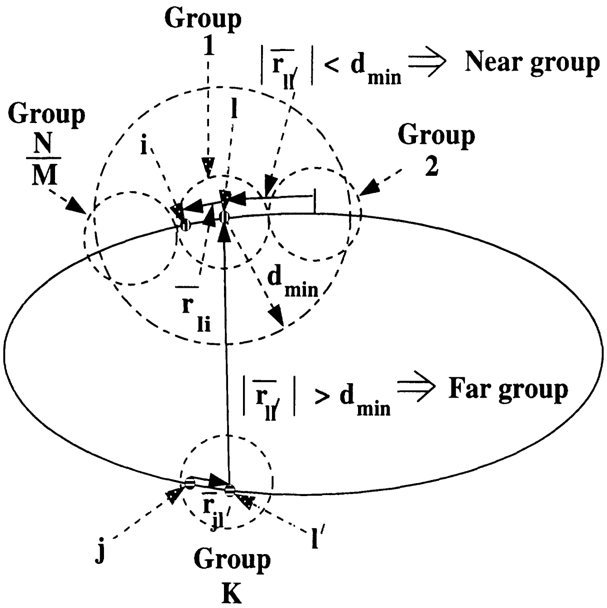

Figure 2: The process of grouping unknowns - two groups are in the near field of each other if the distance between their centers $r_{l'l}$ is less than d_{min}

1. For each test group, the aggregation of source elements in a single source group involves M operations, corresponding to the number of

elements in the source group. The aggregation operation corresponds to

$$b_{l'l} = \sum_{j=1}^{M} I_j e^{-\mathbf{j} k_0 r_{\widehat{l'l}} \cdot \mathbf{r}_{jl'}} \tag{17}$$

2. Since the above aggregation operation needs to be done for all source groups the operation count becomes $O(\frac{N}{M}M) \sim O(N)$, where $\frac{N}{M}$ represents the total number of groups. Also this operation, being dependent only on the test *group* rather than the test *element*, needs to be repeated for $\frac{N}{M}$ test groups leading to a total operation count of $O(\frac{N^2}{M})$ for aggregation.

3. The next step would be a translation operation corresponding to

   $$c_{l'l} = \frac{e^{-\mathbf{j} k_0 r_{l'l}}}{r_{l'l}} b_{l'l} \tag{18}$$

   Since this needs to be done only at the group level, it involves $O(\frac{N^2}{M^2})$ operations for all possible test and source group combinations and is the least computationally intensive step.

4. The final step in the sequence would be the process of disaggregation corresponding to the operation

   $$I_{li} = \sum_{l'=1}^{N/M} c_{l'l} e^{-\mathbf{j} k_0 r_{\widehat{l'l}} \cdot \mathbf{r}_{li}} \tag{19}$$

   Conceptually, this process is the converse of aggregation. Since this operation involves only the source *group* instead of the source *element* it needs to be done for each source group thus implying an $O(\frac{N}{M})$ operation to generate a single row of the matrix-vector product. To generate M rows corresponding to a test group the operation count would be $O(N)$. With $\frac{N}{M}$ test groups, the operation count would be of $O(\frac{N^2}{M})$.

5. The near field operation count being of $O(NM)$ and the far field being $O(\frac{N^2}{M})$ gives a total operation count of

   $$Op.count \sim C_1 NM + C_2 \frac{N^2}{M} \tag{20}$$

   Typically, we can set the elements in each group, $M = \sqrt{N}$ and as a result the total operation count is $O \sim N^{1.5}$.

3 Results

The formulation was first validated for resistive plates. The validating code employed was based on the resistive boundary condition and representation of the fields employing the Stratton-Chu integral equation [9]. Figure 3(b) shows the backscatter RCS of a $1.16\lambda \times 0.85\lambda$ plate in the $\phi = 0^0$ plane for the $\phi\phi$ polarization. Results for a metal plate and a resistive plate with normalized resistivity of $2.12 - j0.2$ are shown and comparison between the two sets of data is very good. Figure 3(c) shows the corresponding plots for the $\theta\theta$ polarization.

To validate the typical nose radome geometry, available scattering data for the Von Karman radome were used for reference. Although, this is a BOR structure, it should be remarked that our formulation was not specialized to this class of geometries. The generating curve for this radome (see figure 4) is given by [10]

$$r = \frac{D}{2\sqrt{\pi}}\left\{\cos^{-1}\left(1-\frac{2z}{L}\right)-\frac{1}{2}\sin\left[2\cos^{-1}\left(1-\frac{2z}{L}\right)\right]\right\}^{\frac{1}{2}} \tag{21}$$

with

$$r = \sqrt{x^2+y^2} \tag{22}$$

and D is the diameter of the radome base whereas L is the length of the radome. The thickness of the dielectric shell was $h = 0.05m$ and the dielectric constant was $\epsilon_r = 4.0$. The resistive sheet condition $(R = \frac{-j}{k_0(\epsilon_r-1)h})$ gives an equivalent resistivity of -j1.061. Discretization of this geometry at twelve points/wavelength, results in 187 nodes, 362 triangular facets and 549 edges (unknowns) as shown in figure 4(b). The bistatic RCS with nose-on incidence is shown in figure 4(c) and (d). Also shown in these figures is the comparison with a surface integral formulation [2]. As seen there is very good agreement between the two codes even though the RCS levels are very low at angles away from forward scattering.

The incorporation of the fast algorithm alleviates the limitation on the size of the bodies analyzed as can be inferred from the results shown in figure 5. In this figure a metallic nose radome 10λ long with a circular base of diameter of 1λ is analyzed. Again, a body of revolution was the geometry of choice because of the availability of validation data from CICERO [11]. Discretization of this radome results in 3120 nodes and 6204 triangular facets.

Comparison of the backscatter RCS from the two codes (see figure 5) reveals very good agreement for the $\theta\theta$ polarization while the $\phi\phi$ polarization shows some deviation particularly at the low RCS levels. The near group radius employed in the FMM solution was 2λ and the number of unknowns was 9324. Solution times were 12 seconds/iteration for the FMM radome code while the conjugate gradient solver employing the full, unreduced system would need an estimated 60 seconds/iteration. Estimates from scaling smaller problems indicate that LU decomposition would need a solution time of about five and a half hours while requiring an unrealistic 0.67 GB of memory for storage of the full matrix.

An important advantage of integral equation analysis for the nose radome problem is that it avoids modeling the free space between the radome and nose antenna (see figures 6 - 9) thus reducing the computational cost. Results which include the interactions between the nose-antenna and the radome are given in figures 6 - 9. Unlike the Von Karman radome which was generated by an algebraic equation, the radome in figures 6 - 9 was generated from user specified elliptical or circular cross sections, which were then interpolated with cubic splines to generate the cross section at any intermediate point along the axis. Figure 8 depicts the $\sigma_{\theta\theta}$ backscatter cross-section of the dielectric nose radome alone and in the presence of a circular plate at the base of the radome (nose antenna). The antenna is inclined with respect to the plane perpendicular to the radome axis. The effect of the antenna on the RCS is pronounced at incidence angles close to specular directions of the antenna plate and this was to be expected. This is particularly seen in figure 8 for the backscatter RCS patterns perpendicular to the plane with respect to which the antenna is inclined. Specifically the large peak observed in figure 8 at $\phi = 150^0$ when the antenna is inclined at 60^0 with respect to the x-z plane is due to the large specular return at that angle of incidence.

4 Conclusion

A version of the fast multipole method was employed to compute the electromagnetic scattering from electrically large nose radome structures. The application of this technique while preserving to a great extent the accuracy of the moment method, significantly alleviates the limitations on the size of the bodies analyzed. In this work we analyzed nose radome shaped structures which were composed of metal or thin dielectric shells and in the case of the latter the resistive boundary condition was employed. The hybridization of a technique such as the finite element method will enable the treatment of a wider class of materials and could thus handle radomes with frequency selective surfaces. The application of such a technique to scattering from material filled grooves has already been discussed in [12],[13].

References

[1] Y.T. Lo and S.W. Lee ed., *Antenna handbook*, Van Nostrand, New York, 1988.

[2] E. Arvas and S. Ponnapalli, Scattering cross section of a small radome of arbitrary shape, *IEEE Trans. Antennas Propagat.*, 37(5):655-658, May 1989.

[3] V. Rokhlin, Rapid solution of integral equations of scattering theory in two dimensions, *J. Comput. Phys.*, 86(2):414-439, 1990.

[4] T.B.A. Senior and J.L. Volakis, *Approximate boundary conditions in electromagnetics*, IEE press, London, 1995.

[5] S.M. Rao, D.R. Wilton, and A.W. Glisson, Electromagnetic scattering by surfaces of arbitrary shape, *IEEE Trans. Antennas Propagat.*, 30(3):409-418, May 1982.

[6] D.R. Wilton, S.M. Rao, A.W. Glisson, D.H. Schaubert, O.M. Al-Bundak, and C.M. Butler, Potential integrals for uniform and linear source distributions on polygonal and polyhedral domains, *IEEE Trans. Antennas Propagat.*, 32:276-281, March 1984.

[7] C.C. Lu and W.C. Chew, Fast far field approximation for calculating the RCS of large objects, *Micro. Opt. Tech. Lett.*, 8(5):238-241, April 1995.

[8] S.S. Bindiganavale and J.L. Volakis, Guidelines for using the fast multipole method to calculate the RCS of large objects, *Micro. Opt. Tech. Lett.*, March 1996.

[9] M. Naor and T.B.A. Senior, Scattering by resistive plates, Radiation Laboratory Technical Report# 018803-1-T, Ann Arbor MI, Sept. 1981.

[10] J.D. Walton ed., *Radome engineering handbook*, Marcel Dekker, New York, 1970.

[11] J.M Putnam and L.N. Medgyesi-Mitschang, Combined field integral equation formulation for axially inhomogeneous bodies of revolution, McDonnell Douglas research laboratories, December 1987.

[12] S.S. Bindiganavale and J.L. Volakis, A hybrid FEM-FMM technique for electromagnetic scattering, To be presented at *ACES 1996 Symposium*, Monterrey CA, March 1996.

[13] S.S. Bindiganavale and J.L. Volakis, A hybrid FEM-FMM technique for electromagnetic scattering, Radiation Laboratory Technical Report# 033762-1-T, Ann Arbor MI, Jan 1996.

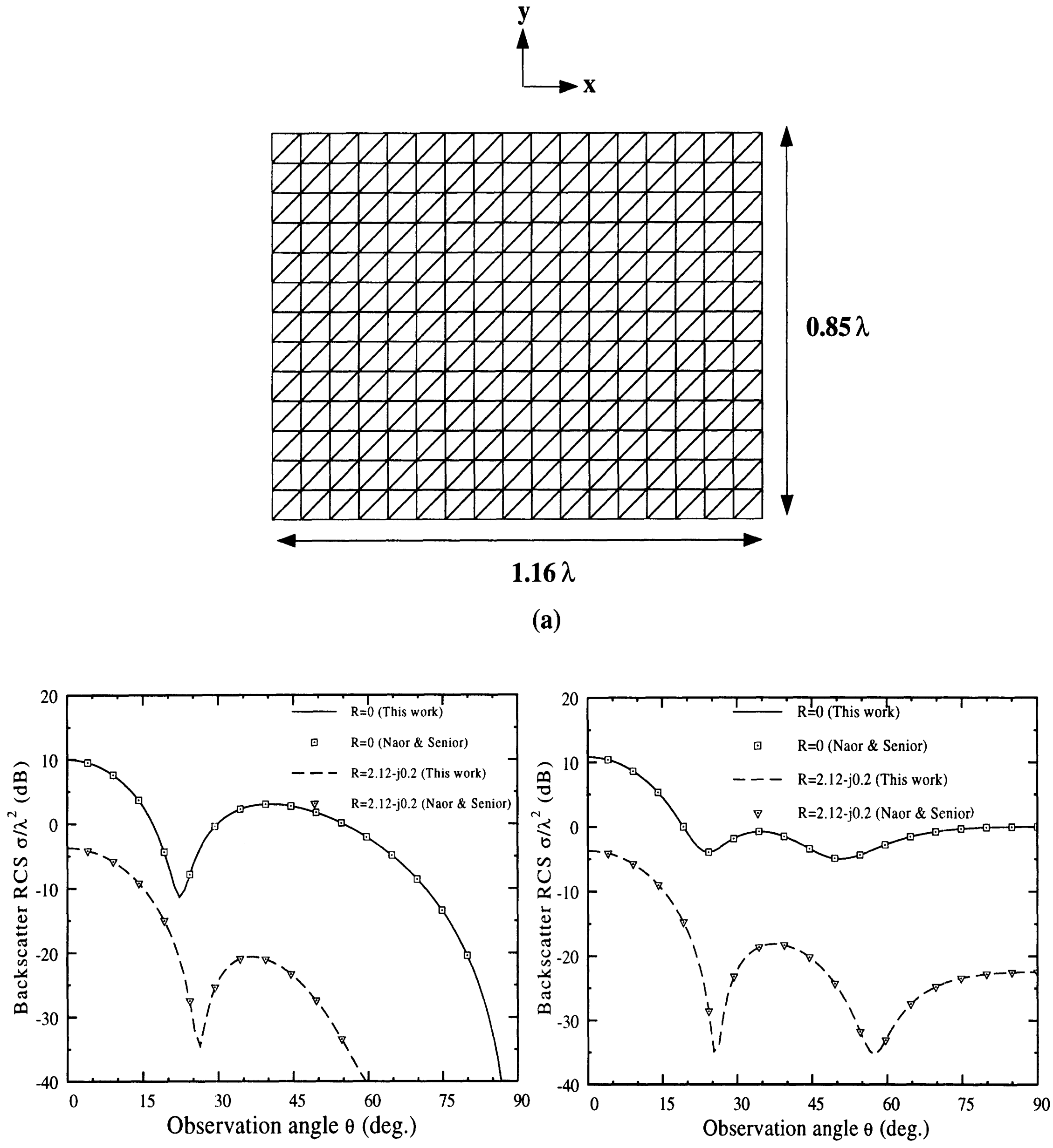

(a)

(b)

(c)

Figure 3: (a) Resistive plate geometry (b) Elevation plane backscatter RCS ($\phi\phi$ polarization) (c) Elevation plane backscatter RCS ($\theta\theta$ polarization)

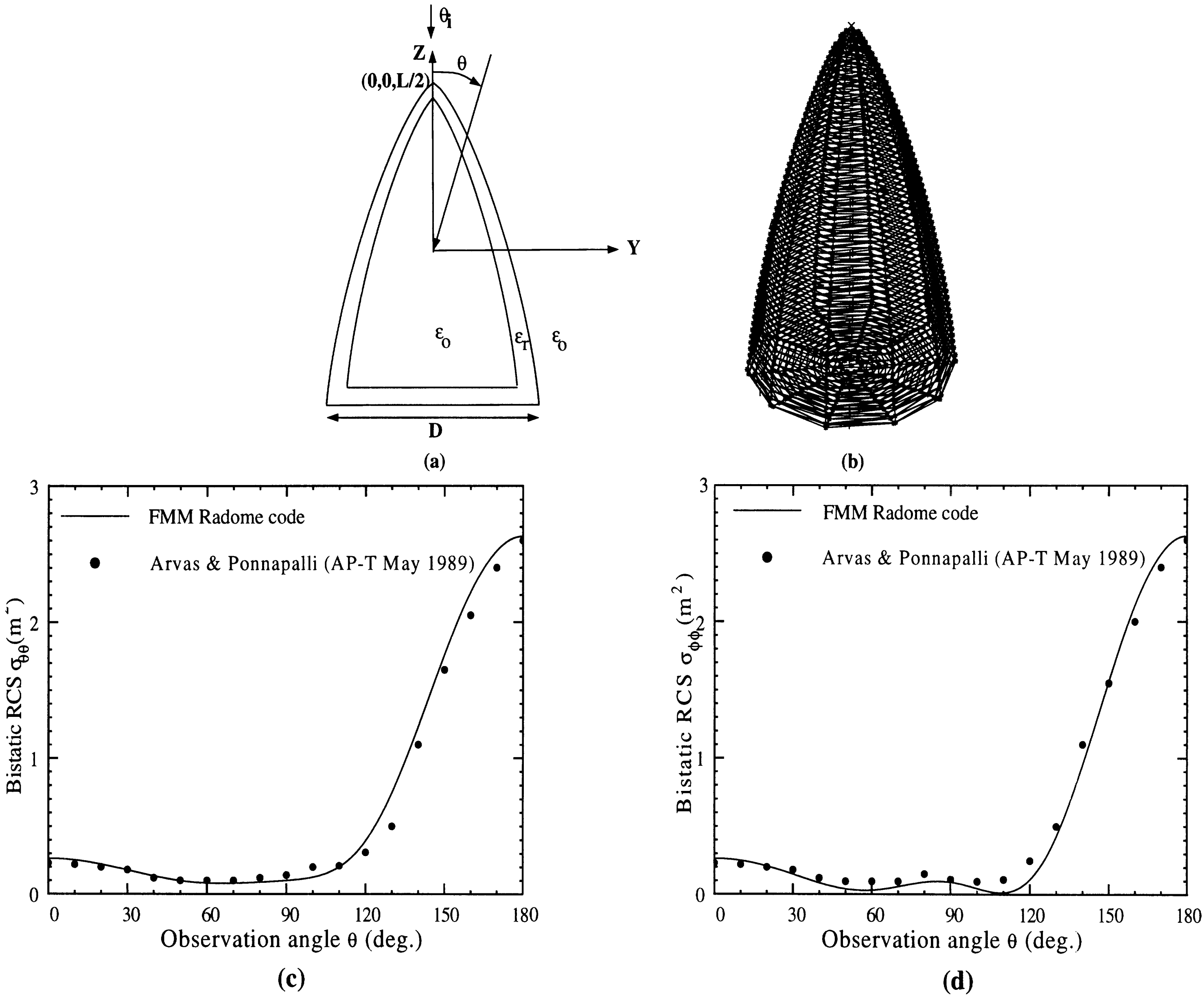

Figure 4: (a) Von Karman radome geometry (2D section) - L = 1.1 m, D = 0.6 m (b) Meshed Von Karman radome (c) Bistatic RCS ($\theta_i = 0^0$) - $\theta\theta$ polarization (d) Bistatic RCS ($\theta_i = 0^0$) - $\phi\phi$ polarization

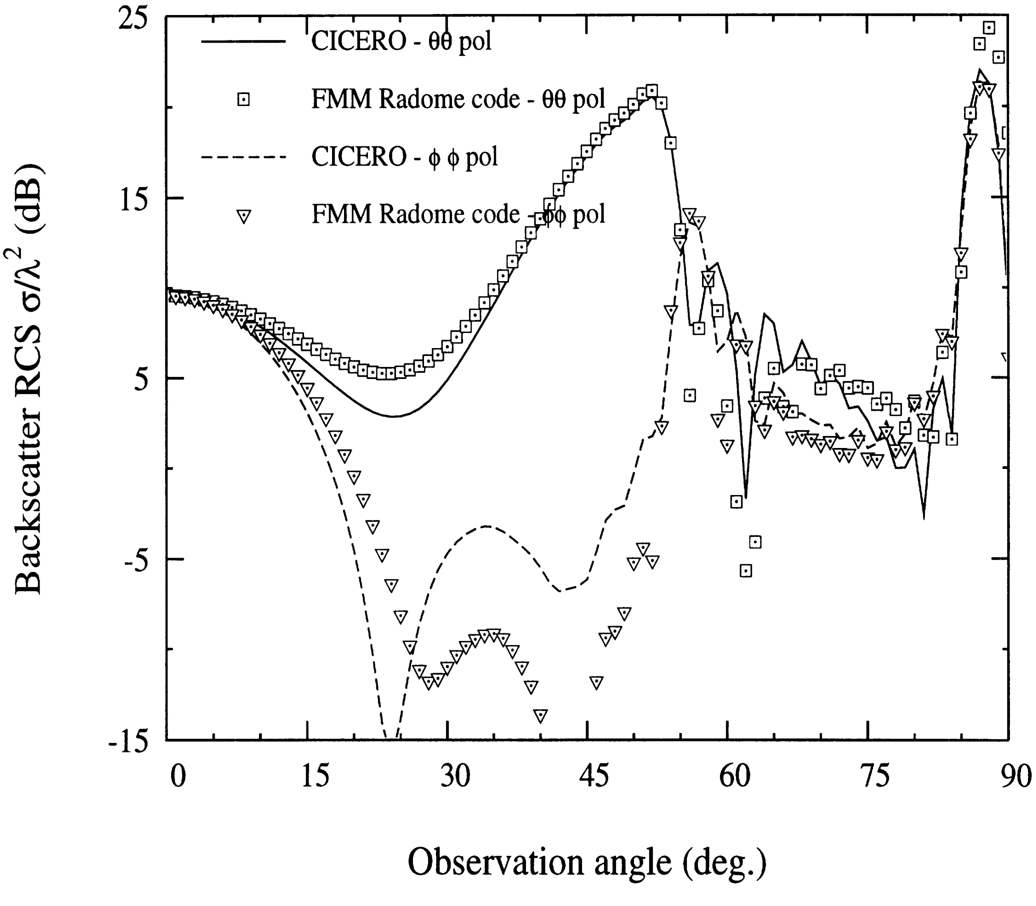

Figure 5: Backscatter RCS for a 10λ long nose radome of diameter 1λ

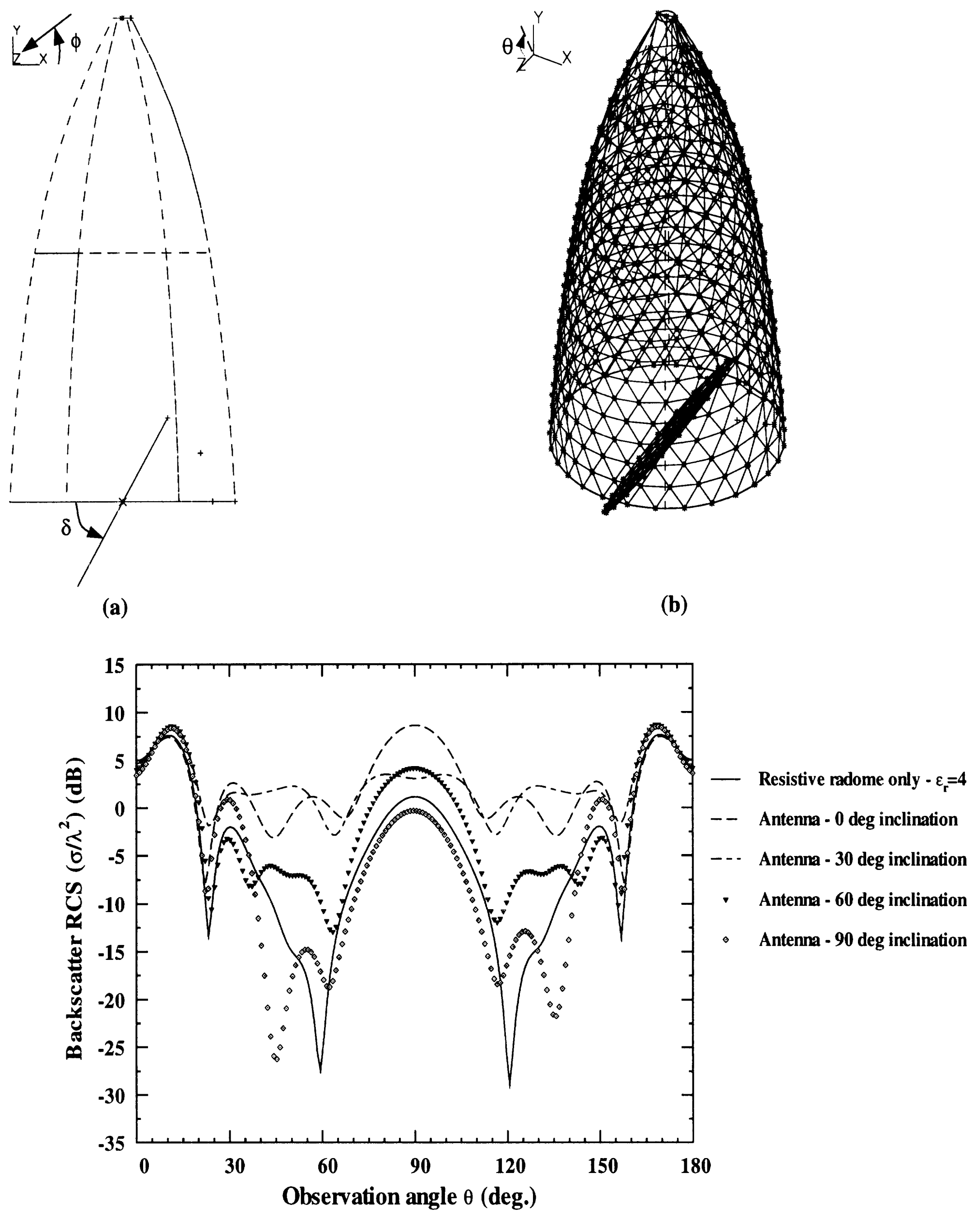

(a) (b)

(c)

Figure 6: (a) and (b) Nose antenna - radome geometry - δ is the angle of antenna inclination w.r.t x-z plane (c) $\sigma_{\theta\theta}$ backscatter RCS (y-z plane)

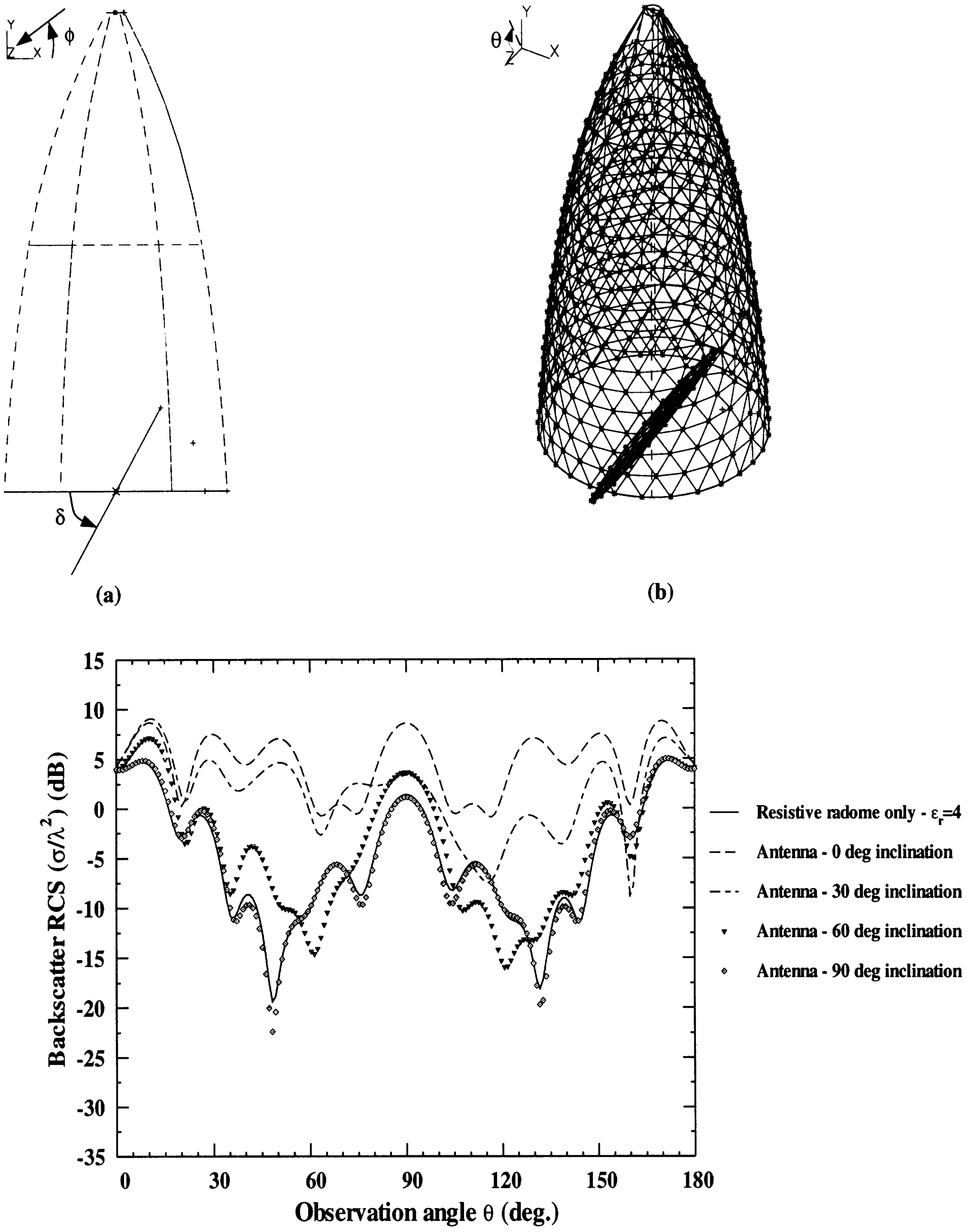

(a)

(b)

(c)

Figure 7: (a) and (b) Nose antenna - radome geometry - δ is the angle of antenna inclination w.r.t x-z plane (c) $\sigma_{\phi\phi}$ backscatter RCS (y-z plane)

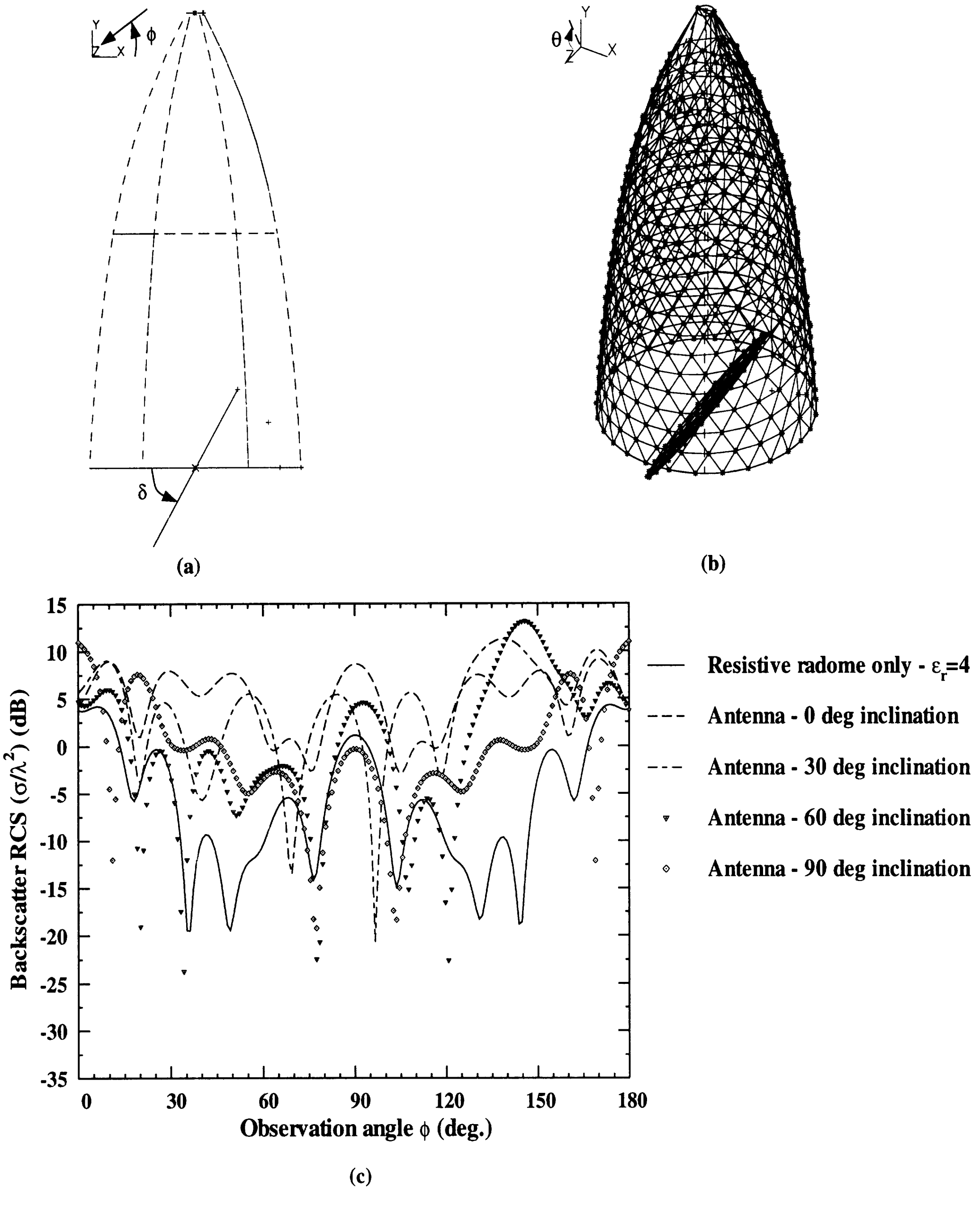

(a)

(b)

(c)

Figure 8: (a) and (b) Nose antenna - radome geometry - δ is the angle of antenna inclination w.r.t x-z plane (c) $\sigma_{\theta\theta}$ backscatter RCS (x-y plane)

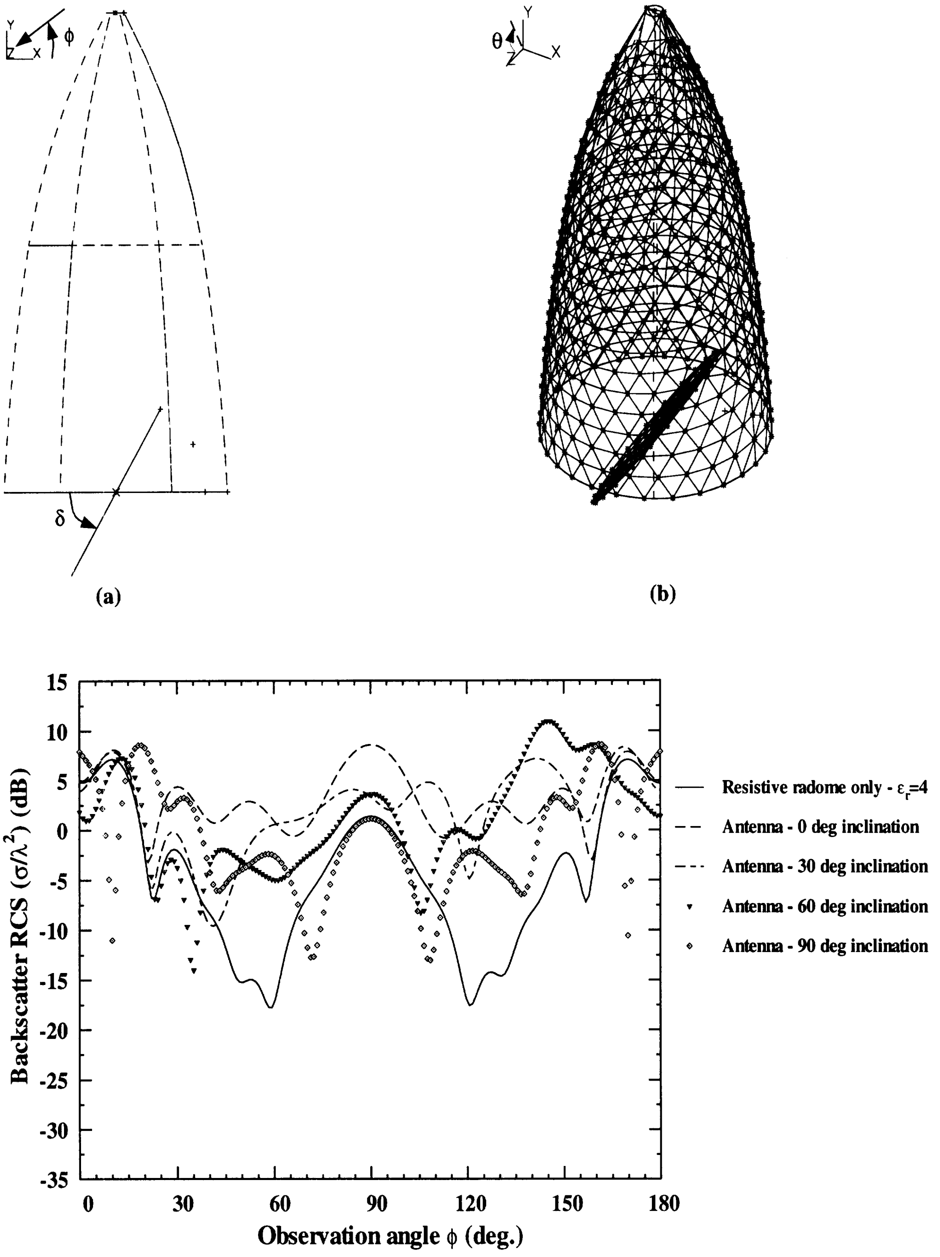

(a) (b)

(c)

Figure 9: (a) and (b) Nose antenna - radome geometry - δ is the angle of antenna inclination w.r.t x-z plane (c) $\sigma_{\theta\theta}$ backscatter RCS (x-y plane)